

# Signatures of the Core-Powered Mass-Loss Mechanism in the Exoplanet Population: Dependence on Stellar Properties and Observational Predictions

Akash Gupta<sup>1\*</sup> and Hilke E. Schlichting<sup>1,2</sup>

<sup>1</sup>*Department of Earth, Planetary, and Space Sciences, University of California, Los Angeles, CA 90095, USA*

<sup>2</sup>*Department of Earth, Atmospheric and Planetary Sciences, Massachusetts Institute of Technology, MA 02139, USA*

Accepted XXX. Received YYY; in original form ZZZ

## ABSTRACT

Recent studies have shown that atmospheric mass-loss powered by the cooling luminosity of a planet’s core can explain the observed radius valley separating super-Earths and sub-Neptunes, even without photoevaporation. In this work, we investigate the dependence of this core-powered mass-loss mechanism on stellar mass ( $M_*$ ), metallicity ( $Z_*$ ) and age ( $\tau_*$ ). Without making any changes to the underlying planet population, we find that the core-powered mass-loss model yields a shift in the radius valley to larger planet sizes around more massive stars with a slope given by  $d \log R_p / d \log M_* \simeq 0.35$ , in agreement with observations. To first order, this slope is driven by the dependence of core-powered mass-loss on the bolometric luminosity of the host star and is given by  $d \log R_p / d \log M_* \simeq (3\alpha - 2)/36 \simeq 0.36$ , where  $(L_*/L_\odot) = (M_*/M_\odot)^\alpha$  is the stellar mass-luminosity relation and  $\alpha \simeq 5$  for the CKS dataset. We therefore find, contrary to photoevaporation models, no evidence for a correlation between planet and stellar mass. In addition, we show that the location of the radius valley is, to first order, independent of stellar age and metallicity. In contrast, assuming that the atmospheric opacity scales linearly with stellar metallicity, we determine that the size of sub-Neptune population increases with metallicity and decreases with age with a slope given by  $d \log R_p / d \log Z_* \simeq 0.1$  and  $d \log R_p / d \log \tau_* \simeq -0.1$ , respectively. This implies that the abundance of super-Earths relative to sub-Neptunes increases with age but decreases with stellar metallicity. We conclude with a series of observational tests that can differentiate between core-powered mass-loss and photoevaporation models.

**Key words:** planets and satellites: atmospheres – planets and satellites: formation – planets and satellites: physical evolution – planets and satellites: gaseous planets – planets and satellites: composition – planet-star interactions

## 1 INTRODUCTION

In the last decade, NASA’s *Kepler* mission has revolutionized the field of exoplanets by discovering more than 4000 planetary candidates (e.g., Borucki et al. 2010). These discoveries offer new insights into the formation and evolution of planets. One of *Kepler*’s key findings is that the most common planets, observed to date, are one to four Earth radii ( $R_\oplus$ ) in size (e.g., Fressin et al. 2013; Petigura et al. 2013). In addition, transit-timing variations (e.g., Carter et al. 2012; Hadden & Lithwick 2017) and follow-up radial velocity (e.g., Marcy et al. 2014b; Weiss & Marcy 2014) measurements have revealed that planets smaller than about  $1.6 R_\oplus$  have higher densities suggesting rocky ‘Earth-like’

compositions while larger planets have lower densities consistent with significant H/He envelopes (e.g., Marcy et al. 2014a; Rogers 2015). Intriguingly, analyses of early photometry data from the *Kepler* Input Catalog (e.g., Brown et al. 2011), the recent spectroscopic follow-up of planet-hosting stars by the California-*Kepler* Survey (CKS; Petigura et al. 2017), and the latest studies incorporating *Gaia* astrometry and asteroseismology-based data have all revealed a ‘radius valley’ in the distribution of these small, close-in (orbital period  $< 100$  days) exoplanets (e.g., Owen & Wu 2013; Lopez & Fortney 2013; Fulton et al. 2017; Fulton & Petigura 2018; Van Eylen et al. 2018; Berger et al. 2018; Martinez et al. 2019).

This radius valley marks the transition from a population of small, rocky ‘super-Earths’ to a population of large ‘sub-Neptunes’ with significant H/He envelopes (e.g., Owen

\* E-mail: akashgpt@ucla.edu

& Wu 2013; Lopez & Fortney 2013, 2014; Rogers 2015; Ginzburg et al. 2016). Furthermore, studies involving *Gaia* astrometry (Martinez et al. 2019) and asteroseismology-based high-precision measurements (Van Eylen et al. 2018) of stellar parameters have measured the slope of the radius valley and obtained values of  $d \log R_p / d \log M_* = -0.11^{+0.03}_{-0.03}$  and  $-0.09^{+0.04}_{-0.02}$ , respectively.

The bimodality in the radius distribution has been attributed to photoevaporation of H/He envelopes by high-energy radiation (e.g., XUV) from the host stars (e.g., Owen & Wu 2013; Lopez & Fortney 2013; Jin et al. 2014; Chen & Rogers 2016; Owen & Wu 2017; Jin & Mordasini 2018). Under this mechanism, close-in planets can receive, over a lifetime, a total time-integrated high-energy flux comparable to their atmosphere’s binding energy and are thus able to lose their atmospheres (e.g., Owen & Wu 2017). Studies have demonstrated that planetary evolution with photoevaporation can reproduce the radius valley. In addition, these studies infer ‘Earth-like’ bulk composition of the planetary cores implying a low overall water-fraction (e.g., Owen & Wu 2017; Jin & Mordasini 2018; Wu 2019).

Recently, Ginzburg et al. (2018) and Gupta & Schlichting (2019) showed that the core-powered mass-loss mechanism is also able to reproduce the observed radius valley, even in the absence of photoevaporation. In this mechanism, a planet’s internal luminosity drives the loss of its atmosphere (Ginzburg et al. 2016, 2018; Gupta & Schlichting 2019). The source of this luminosity is a planet’s primordial energy from formation, which can be of the order of, or even larger than, its atmosphere’s gravitational binding energy. Gupta & Schlichting (2019) showed that evolution of planets under the core-powered mass-loss mechanism around ‘Sun-like’ stars successfully reproduces the location, shape and slope of the radius valley as a function of orbital period. They also demonstrated that the exact location of the radius valley depends on the bulk composition of the planetary cores whereas the relative abundance of super-Earths and sub-Neptunes depends on the underlying planet mass distribution. Similar to photoevaporation studies, Gupta & Schlichting (2019) found that the observations are consistent with ‘Earth-like’ cores with a maximum water-fraction of  $\sim 20\%$ .

New observations provide us with the opportunity to characterize the super-Earth and sub-Neptune populations as a function of their host star properties (e.g., Fulton & Petigura 2018; Petigura et al. 2018; Dong et al. 2018). This opens new avenues to investigate and contrast possible signatures the core-powered mass-loss mechanism and photoevaporation imprint on the exoplanet population (e.g., Owen & Murray-Clay 2018; Wu 2019).

Fulton & Petigura (2018) and Wu (2019) have found that the radius valley increases in planet size with stellar mass. Moreover, Fulton & Petigura (2018) found that the planet size distribution also shifts to higher insolation flux with increasing stellar mass.

In addition, Petigura et al. (2018) have reported that the relative occurrence of sub-Neptunes increases with increasing stellar metallicity while the relative occurrence of super-Earths remains largely unchanged; see also Dong et al. (2018). Furthermore, Dong et al. (2018) and Owen & Murray-Clay (2018) have reported that sub-Neptunes are

larger around higher metallicity FGK stars; see also Petigura et al. (2018). Hirano et al. (2018) reported a similar trend in the distribution of planet sizes around M-dwarfs.

Furthermore, studies based on the Zodiocal Exoplanets in Time (ZEIT) survey have reported a trend in planet size with stellar age (e.g., Mann et al. 2016; Rizzuto et al. 2018). Most *Kepler* planets are older than a Gyr and have significant uncertainties in their age estimates. This makes it difficult to investigate any trends in planet size with stellar age. However, observations from the *K2* mission have allowed the discovery of planets in young clusters like Praesepe and Hyades, both of which are about 650 million years old (e.g., Mann et al. 2016; Rizzuto et al. 2018). The number of planets observed in such clusters is still below ten and thus not statistically significant, nevertheless, these younger planets are bigger, on average, than their older *Kepler* counterparts; see Figure 12 in Rizzuto et al. (2018).

In this work, we extended previous work on the core-powered mass-loss mechanism (Ginzburg et al. 2018; Gupta & Schlichting 2019), and investigated how stellar mass, metallicity and age impact the resulting planet size distribution. We model our host star population on the stars in the CKS survey and investigate, collectively and in isolation, the impact of stellar mass, metallicity and age on the resulting exoplanet size distribution. We show that core-powered mass-loss can explain many of the observational trends with stellar properties discussed above. In addition, we quantify how different stellar properties shape the observed planet size distribution. Contrary to photoevaporation models, we find no evidence for a correlation between planet and stellar mass and show that the observed dependence of the radius valley on stellar mass is, to first order, driven by the stellar mass-luminosity relation.

This paper is structured as follows: In Section 2, we describe the core-powered mass-loss mechanism and discuss our model for planetary structure and composition. We then explain, in Section 3, how we model the exoplanet and stellar populations. The numerical and analytical core-powered mass-loss results are divided into two sections. In Section 4, we present a comparison of our results with the current exoplanet observations. Complementing that, in Section 5, we show how the core-powered mass-loss mechanism depends on the individual stellar properties, make predictions for trends with stellar mass, metallicity and age and investigate if there is any correlation between planet and stellar mass. Finally, we summarize our results in Section 6 and present observational tests for distinguishing between the signatures of core-powered mass-loss and photoevaporation.

## 2 PLANET STRUCTURE AND EVOLUTION UNDER THE CORE-POWERED MASS-LOSS MECHANISM

To study the imprint of the core-powered mass-loss mechanism on the exoplanet population, we solely focus on core-powered mass neglecting mass-loss due to photoevaporation and other mechanisms. For a detailed review of this mechanism, we refer the reader to Ginzburg et al. (2016) and for its dependence on planetary properties, to Gupta & Schlichting (2019).

As a planetary core grows by accreting solids, gravita-

tional binding energy is converted into heat. This thermal energy can be efficiently radiated away if the core forms in isolation. However, if this accretion occurs in the presence of a gas disk, then the core will start accreting a H/He envelope from the surrounding nebula once its Bondi radius is larger than its physical radius. The presence of an optically thick envelope acts as a ‘thermal blanket’ since, from this point onward, the core’s heat loss is limited by the thermal diffusion across the radiative-convective boundary of the envelope (e.g. Lee & Chiang 2015; Ginzburg et al. 2016), significantly reducing the cooling rate of the underlying core. As a result, the core temperature is essentially set by the maximum temperature that permits the accretion of a H/He envelope and is roughly given by  $T_c \sim GM_c \mu / k_B R_c$ , where  $\mu$  is the mean molecular mass of the atmosphere,  $k_B$  is the Boltzmann constant,  $G$  is the gravitational constant and  $M_c$  and  $R_c$  are the mass and radius of the planetary core, respectively. This implies typical core temperatures of  $10^4$  -  $10^5$  K for core masses ranging from the mass of Earth to Neptune. It is this primordial energy from planet formation that drives atmospheric loss in the core-powered mass-loss mechanism which proceeds over Gyr timescales.

As the protoplanetary disk disperses, it causes a loss of pressure support on the outside of the planet’s atmosphere. As a consequence, the planet experiences ‘spontaneous’ atmospheric mass-loss driven by the luminosity of the inner regions of its atmosphere (Ginzburg et al. 2016; Owen & Wu 2016). Due to this atmospheric mass-loss, the atmosphere rapidly shrinks to a few times the planet’s core radius over the disk dispersal timescale. This sets the initial condition for planetary evolution under the core-powered mass-loss and photoevaporation (Owen & Wu 2017) mechanisms.

At this stage, we assume that a typical planet with radius  $R_p$  and mass  $M_p$  has a dense core of radius  $R_c$  and mass  $M_c$ , and a surrounding gaseous atmosphere of mass  $M_{atm}$ . We define the core as the non-gaseous part of the planet which dominates the planet’s mass such that  $M_c \sim M_p$ . We account for gravitational compression by assuming that the mass-radius relation of the core is given by  $M_c/M_\oplus = (R_c/R_\oplus)^4 (\rho_{c*}/\rho_\oplus)^{4/3}$ , where  $\rho_{c*}$  is the density of the core scaled to an Earth mass and  $\oplus$  refers to the corresponding Earth values (Valencia et al. 2006; Fortney et al. 2007). Motivated by direct observational measurements of super-Earth masses and radii (see Figure 10 from Bower et al. 2019, and references therein) and previous core-powered mass-loss results (Gupta & Schlichting 2019), we assume throughout this paper a density of  $\rho_{c*} = 5.0 \text{ g cm}^{-3}$  for the cores, when scaled to an Earth mass. This density estimate is 10% lower than that used by Gupta & Schlichting (2019) but is in better agreement with the radius distribution observations from Fulton & Petigura (2018) when considering a distribution of planet host stars modelled after the CKS-II dataset (Johnson et al. 2017, see Section 3.2 for more details). In addition we model the core as incompressible, molten and fully convective, and assume that the core-envelope interface is well-coupled.

Motivated by previous work on gas accretion and loss during disk dispersal (Ginzburg et al. 2016), we model all planets with an initial atmosphere to core mass-fraction ( $f$ ) given by

$$f \simeq 0.05(M_c/M_\oplus)^{1/2}. \quad (1)$$

We assume that all planets have initial  $H_2$  envelopes and that they can be described as a diatomic ideal gas with  $\gamma = 7/5$  and  $\mu = 2 \text{ amu}$ . Although the initial atmosphere to core mass-fraction is only a few percent, the presence of the atmosphere significantly increases the size of the planet. Following past works (Piso & Youdin 2014; Lee & Chiang 2015; Inamdar & Schlichting 2015), we assume that the atmosphere is structured such that it has an inner convective and outer isothermal region. The convective region is modeled to be adiabatic and contains most of the atmospheric mass while the radiative region is close to isothermal. The atmosphere transitions from the convective to radiative region at the radiative-convective boundary,  $R_{rcb}$ . We assume that the planet size is given by the radiative-convective boundary, i.e.,  $R_p \sim R_{rcb}$ , since the atmospheric density decreases exponentially outside the  $R_{rcb}$ . In other words, we assume that the atmospheric thickness is  $\Delta R \sim R_{rcb} - R_c$ , where  $\Delta R$  initially is a few  $R_c$ .

The aforementioned model yields an atmospheric mass of

$$M_{atm} = \frac{\gamma - 1}{\gamma} 4\pi R_c^2 \rho_{rcb} \Delta R \left( \frac{R'_B \Delta R}{R_c^2} \right)^{1/(\gamma-1)}. \quad (2)$$

Here  $\gamma$  is the ratio of heat capacities for the atmosphere,  $\rho_{rcb}$  is the density of the atmosphere at the  $R_{rcb}$  and  $R'_B$  is the modified Bondi radius, such that

$$R'_B \equiv \frac{\gamma - 1}{\gamma} \frac{GM_c \mu}{k_B T_{rcb}}, \quad (3)$$

where  $T_{rcb}$  is the temperature at the  $R_{rcb}$ .  $T_{rcb}$  is approximately the planetary equilibrium temperature,  $T_{eq}$ , for a given distance from the host star which can be written as

$$T_{eq} = \left( \frac{1}{16\pi\sigma} \frac{L_*}{a^2} \right)^{1/4}, \quad (4)$$

where  $\sigma$  is the Stefan-Boltzmann constant,  $a$  is the planet’s semi-major axis and  $L_*$  is the luminosity of the host star. To facilitate direct comparison with observations, we present some of our results as a function of stellar insolation flux,  $S$ , which is related to the equilibrium temperature by  $S/S_\oplus = (T_{eq}/T_{eq,\oplus})^4$ .

The total energy available for cooling ( $E_{cool}$ ) is the sum of the thermal energy in the atmosphere and core and the atmosphere’s gravitational energy, i.e.

$$E_{cool} \simeq g\Delta R \left( \frac{\gamma}{2\gamma - 1} M_{atm} + \frac{1}{\gamma} \frac{\gamma - 1}{\gamma_c - 1} \frac{\mu}{\mu_c} M_c \right), \quad (5)$$

where  $\mu_c$  and  $\gamma_c$  are the molecular mass and adiabatic index of the core, and  $g = GM_c/R_c^2$ . Since the core-envelope interface is well coupled, the cooling of both the core and atmosphere is dictated by the radiative diffusion through the radiative-convective boundary, and thus the luminosity of the planet is

$$L = -\frac{dE_{cool}}{dt} = \frac{64\pi}{3} \frac{\sigma T_{rcb}^4 R'_B}{\kappa \rho_{rcb}}, \quad (6)$$

where  $\kappa$  is the opacity at the radiative-convective boundary. We assume that this opacity scales as

$$\frac{\kappa}{0.1 \text{ cm}^2 \text{ g}^{-1}} = \frac{Z_*}{Z_\odot} \left( \frac{\rho_{rcb}}{10^{-3} \text{ g cm}^{-3}} \right)^\beta \quad (7)$$

where  $Z_*$  is the stellar metallicity,  $Z_\odot$  the metallicity of the

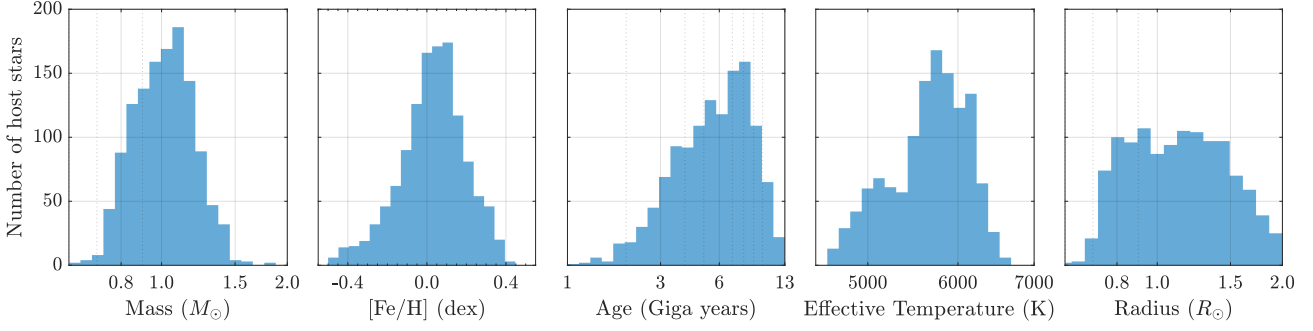


**Figure 1.** Distributions of stellar properties from CKS-II dataset (Petigura et al. 2017; Johnson et al. 2017).

Sun and  $\beta$  is assumed to be 0.6 throughout this paper (e.g., Lee & Chiang 2015; Freedman et al. 2008). Here we are assuming that the observed stellar metallicities are representative of the metallicity of the planetary atmospheres which, in turn, are directly proportional to atmospheric opacities such that  $[\text{Fe}/\text{H}] = [Z_*/Z_\odot]$ .

Combining eqs. (5) and (6) yields a planetary cooling timescale given by

$$t_{cool} = \frac{E_{cool}}{|dE_{cool}/dt|} = \frac{E_{cool}}{L}. \quad (8)$$

There are two regimes of atmospheric mass-loss: energy-limited mass-loss and Bondi-limited mass-loss. The energy-limited mass-loss rate is

$$\dot{M}_{atm}^E \approx \frac{L(t)}{gR_c}, \quad (9)$$

i.e., it is the absolute upper limit on the atmospheric mass-loss rate achievable assuming all the cooling luminosity goes into driving the mass-loss. On the other hand, the Bondi-limited mass-loss rate,  $\dot{M}_{atm}^B$ , signifies a physical limit on the atmospheric mass-loss rate dictated by the thermal velocity of the gas molecules at the Bondi radius (e.g., Ginzburg et al. 2016; Owen & Wu 2016). Because the hydrodynamic outflow of the atmosphere has to pass through the sonic point and since the mass flux is conserved, it is convenient to determine the mass-loss rate at the sonic point,  $R_s = GM_p/2c_s^2$ , where  $c_s = (k_B T_{eq}/\mu)^{1/2}$  is the isothermal speed of sound. In this case, the mass-loss rate is  $\dot{M} = 4\pi\rho_s R_s^2 c_s$ , where  $\rho_s$  is the density at the sonic point. In the limit that  $R_s \gg R_{rcb}$ ,  $\rho_s$  is related to the density at the radiative-convective boundary by  $\rho_s = \rho_{rcb} \exp(-2R_s/R_{rcb})$ . The mass-loss rate at the Bondi radius is therefore given by

$$\dot{M}_{atm}^B = 4\pi R_s^2 c_s \rho_{rcb} \exp\left(-\frac{GM_p}{c_s^2 R_{rcb}}\right). \quad (10)$$

The actual atmospheric mass-loss rate is the minimum of the energy-limited and Bondi-limited mass-loss rates, i.e.,  $\dot{M}_{atm} = \min\{\dot{M}_{atm}^E, \dot{M}_{atm}^B\}$ . Combining Equations (2), (9) and (10) yields an atmospheric mass-loss timescale that can be written as

$$t_{loss} = \frac{M_{atm}}{|dM_{atm}/dt|} = \max\left\{\frac{M_{atm}}{\dot{M}_{atm}^E}, \frac{M_{atm}}{\dot{M}_{atm}^B}\right\}. \quad (11)$$

Planets which eventually become super-Earths have enough energy to lose their atmospheres entirely and have

mass-loss timescales shorter than cooling timescales. On the other hand, sub-Neptunes either do not have enough energy for complete atmospheric loss or have mass-loss timescales that are longer than their cooling timescales or the age of the system.

In our numerical simulations, we simultaneously calculate cooling and atmospheric mass-loss of a planet by evolving the planet's energy and atmospheric mass as

$$E_{cool}(t + dt) = E_{cool}(t) - L(t) dt \text{ and} \quad (12)$$

$$M_{atm}(t + dt) = M_{atm}(t) - \dot{M}_{atm}(t) dt, \quad (13)$$

respectively; using Equations (2), (5), (9) and (10). We chose an integration time step such that  $dt = 10^{-2} \times \min\{t_{cool}, t_{loss}\}$ .

### 3 MODELING THE EXOPLANET POPULATION AND ITS HOST STARS

In this section, we discuss how we model the planetary and stellar populations in our numerical simulations.

#### 3.1 Exoplanet Population

Following previous works (Owen & Wu 2017; Ginzburg et al. 2018; Gupta & Schlichting 2019), we adopt the following orbital period and planet mass distribution to model the exoplanet population:

$$\frac{dN}{d \log P} \propto \begin{cases} P^2, & P < 8 \text{ days} \\ \text{constant}, & P > 8 \text{ days, and} \end{cases} \quad (14)$$

$$\frac{dN}{dM_c} \propto \begin{cases} M_c \exp\left(-M_c^2/(2\sigma_M^2)\right), & M_c < 5 M_\oplus \\ M_c^{-2}, & M_c > 5 M_\oplus. \end{cases} \quad (15)$$

Here,  $\sigma_M$  is the planet mass where the planet mass distribution peaks. Following Gupta & Schlichting (2019), we assume  $\sigma_M = 3M_\oplus$  unless otherwise stated. Throughout this work, we assume that the period distribution is independent of stellar mass, which is, to first order, consistent with observations (Fulton & Petigura 2018).

#### 3.2 Host Star Population

We model the stellar population on the CKS-II dataset (Johnson et al. 2017). We find 1246 host stars in the CKS-II



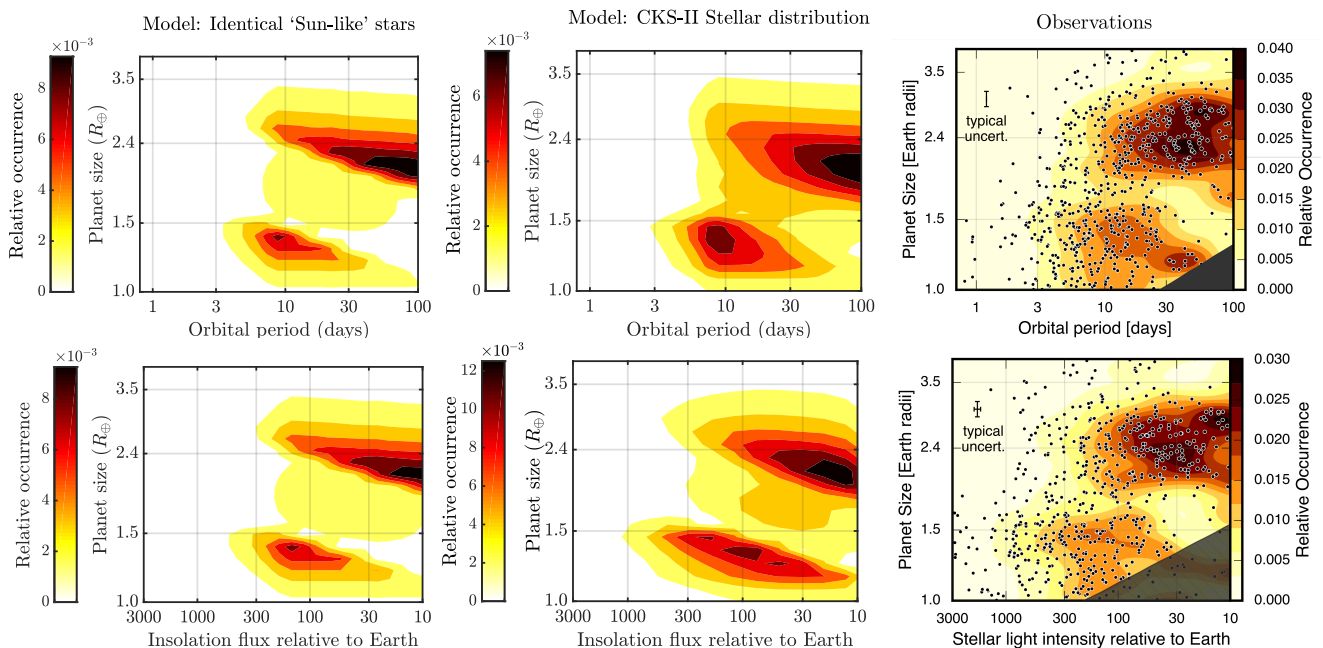


**Figure 2.** Comparison of core-powered mass-loss results with observations. The top row shows planet size as a function of orbital period whereas the bottom row displays planet size as a function of stellar insolation flux. The left panel corresponds to results from [Gupta & Schlichting \(2019\)](#) which were calculated for planets around identical ‘Sun-like’ host stars, the middle panel displays results from this work for planets around host stars that are modeled after the stellar properties of the CKS-II dataset ([Johnson et al. 2017](#)), and the right panel corresponds to the observed planet size distribution from [Fulton & Petigura \(2018\)](#) based on the CKS-II dataset (reproduced with permission).

dataset after excluding those associated with false positive planet detections. We characterize a host star by the following properties: mass ( $M_*$ ), luminosity ( $L_*$ ), metallicity ( $Z_*$ ) and age ( $\tau_*$ ). Figure 1 shows histograms of these stellar properties from the CKS-II dataset. We use these parameters as stellar inputs when numerically modelling a planet’s thermal evolution and mass-loss while further assuming that the age of the planets is well approximated by the age of their host stars. In total, we evolve a population of 10,000 planets with varying periods and masses (see Equations (14) and (15)) around each of the 1246 CKS-II stars.

In addition, in order to understand the impact of the individual stellar parameters on the observable exoplanet population, we also present core-powered mass-loss results where we only vary one of the following parameters: mass, metallicity or age, while keeping everything else the same. For the stellar parameters that we do not vary, we assume  $M_* = 1 M_\odot$ ,  $[Z_*/Z_\odot] = 0.0$  dex and  $\tau_* = 3$  Gyrs. As in the previous case, we evolve a population of 10,000 planets with period and mass distributions given by Equations (14) and (15) around each of the host stars in the population.

#### 4 RESULTS: COMPARISON WITH OBSERVATIONS

In this section, we compare our core-powered mass-loss results with observations of the planet size distribution and its dependence on orbital period, stellar mass and metallicity.

[Ginzburg et al. \(2018\)](#) and [Gupta & Schlichting \(2019\)](#) demonstrated that, for a population of planets around ‘Sun-like’ stars, the core-powered mass-loss mechanism success-

fully reproduces the radius valley observed in the distribution of small, close-in exoplanets. Here, we extend these previous works to account for the actual, observed properties of the host star population. All the results presented in this section are based on a host star population modeled after the stellar properties in CKS-II dataset; see Section 3.2 for details. This facilitates direct comparison between our results and observations based on the CKS-II dataset (e.g., [Fulton & Petigura 2018](#); [Owen & Wu 2017](#); [Wu 2019](#)).

Figure 2 shows a comparison of our core-powered mass loss results for CKS-II host stars (middle panel) with results based on identical ‘Sun-like’ host stars (left-panel; [Gupta & Schlichting 2019](#)) and observations (right-panel; [Fulton & Petigura 2018](#)). The core-powered mass-loss results are in good agreement with observations successfully reproducing the location, shape and slope of the valley, as well as the location and magnitude of the peaks of the exoplanet populations above and below the valley. In addition, comparison of the middle- and left-panel shows that the core-powered mass-loss results for the two stellar populations are similar but, accounting for the true properties of the underlying stellar population (middle panel) reproduces even finer features of the observations (right panel). For example, our new results can reproduce the ‘triangular’ shape of the radius valley seen in the observations (right-panel) better than our previous study that was based on ‘Sun-like’ host stars [Gupta & Schlichting \(2019\)](#). This is due to the range of stellar properties used in this work, which leads to a shallower upper edge of the valley compared to results for planets around identical ‘Sun-like’ stars.

Figure 3 shows the resulting distribution of planet size as a function of stellar mass from our core-powered mass-

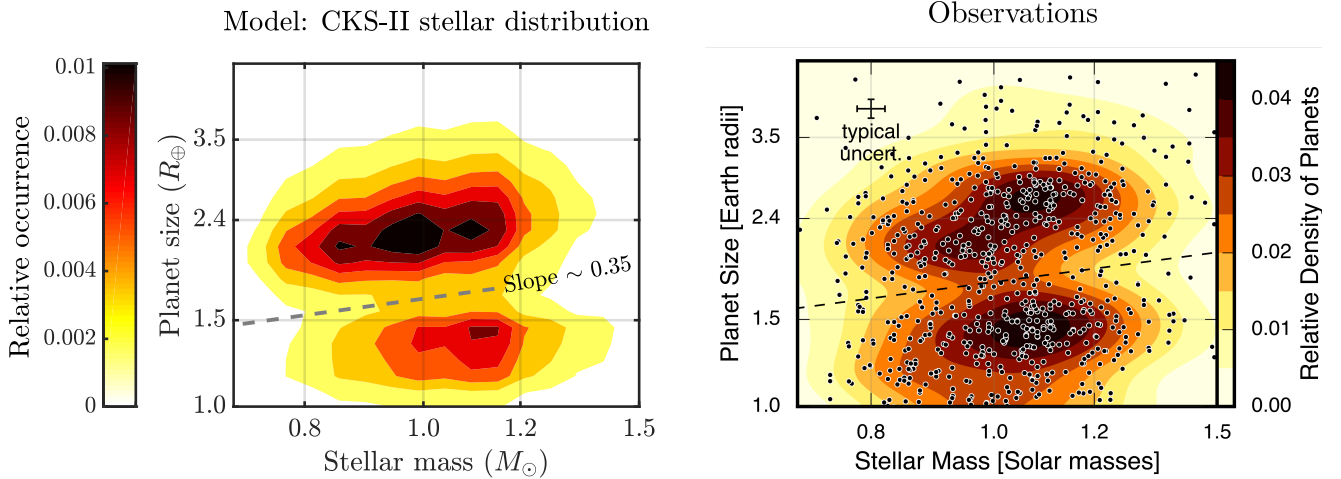


**Figure 3.** Comparison of core-powered mass-loss results (left panel) with observations (right panel) from [Fulton & Petigura \(2018\)](#) (reproduced with permission). The left panel shows the dependence of the core-power mass loss results on stellar mass, demonstrating that larger planetary cores are stripped of their envelopes when residing around more massive host stars compared to planets around lower mass stars. This yields a shift in the valley separating the super-Earth and sub-Neptune populations to larger planet radii for higher mass stars. To first order, this slope is driven by the dependence of the core-powered mass-loss mechanism on the bolometric luminosity of the host star as this dictates the outer boundary condition for atmospheric mass-loss. The dashed lines in both panels indicate the shift in the valley’s location with stellar mass and are plotted with the same slope. *Note:* Completeness corrections associated with observational bias were not accounted for in the right panel (B.J. Fulton, personal communication). Therefore, the relative occurrence of planets above and below the valley cannot be compared with the observations.

loss model (left) and observations from [Fulton & Petigura \(2018\)](#) (right). We find that core-powered mass-loss causes the location of the radius valley and the super-Earth and sub-Neptune populations to increase in planet size with increasing stellar mass. This is consistent with observational results from [Fulton & Petigura \(2018\)](#) and [Wu \(2019\)](#). In addition, we find that the slope of the valley in this parameter space is  $d \log R_p / d \log M_* \sim 0.35$ , which is also in excellent agreement with the values obtained from observations ([Fulton & Petigura 2018](#); [Wu 2019](#)). For example the dashed line in the right panel of Figure 3 from observations by [Fulton & Petigura \(2018\)](#) corresponds to a slope of  $d \log R_p / d \log M_* \sim 0.35$  and [Wu \(2019\)](#) reports a slope of  $d \log R_p / d \log M_* \approx 0.24 - 0.35$  and finds that it extends to M-dwarfs of masses as low as  $0.2 M_\odot$ . We demonstrate in Section 5 that this slope is, to first order, due to the dependence of the core-powered mass-loss mechanism on the bolometric luminosity of the host star as this dictates the outer boundary condition for atmospheric mass-loss.

Figure 4 displays the planet size distribution as a function of period (first row) and insolation (second row) for three stellar mass bins. The observations from [Fulton & Petigura \(2018\)](#) are shown for comparison in rows three and four. Our core-powered mass-loss results (displayed in the first and second row) clearly show that the radius valley moves to larger planet sizes for more massive stars as already shown in Figure 3. In addition, we find that the super-Earth and sub-Neptune populations move to higher stellar insolation for more massive stars. This is due to the fact that the exoplanet period distribution is, motivated by observations (see [Fulton & Petigura \(2018\)](#)), assumed to be independent of stellar mass. As a result, planets with the same orbital period move to higher insolation fluxes around higher mass, i.e. more luminous, stars. For a constant period distribution,

insolation flux scales with stellar mass as  $S \propto M_*^{\alpha-2/3}$ , where  $\alpha$  is the power-law index of the stellar mass-luminosity relation (see Section 5.1 for details). Overall, we find very good agreement between the core-powered mass-loss results and observations. Based on the observational results shown in rows three and four of Figure 4, [Fulton & Petigura \(2018\)](#) reported that the planet size distribution shifts to higher stellar insolation flux around more massive stars and interpret this as a signature of photoevaporation. We question this interpretation based on the core-powered mass-loss results shown in rows one and two of the same figure. As discussed, the shift of the planet size distribution to higher stellar insolation flux around more massive stars is a direct result of the fact that the period distribution is approximately independent of stellar mass. In addition, one needs to be cautious with such claims until the effect of all stellar properties on the results are considered collectively since stellar age and metallicity conspire together such that sub-Neptunes are larger for younger and higher metallicity stars, both of which are correlated with stellar mass in the CKS-II dataset (see Section 5 for details).

In addition, a shift in the exoplanet distribution to higher insolation as a function of stellar type has also been observed around M-dwarfs. [Hirano et al. \(2018\)](#) reported that around early, less XUV active M-dwarfs planets are located at higher insolation flux in comparison to mid-to-late, more XUV active M-dwarfs; see their Figures 18 and 19. [Hirano et al. \(2018\)](#) interpret this as a signature of photoevaporation. However, if this is indeed a signature of photoevaporation transforming sub-Neptunes into super-Earths, then [Hirano et al. \(2018\)](#) should also have found rocky super-Earths at higher insolation around the more active M-dwarfs, as they are the remnants of the stripped sub-Neptunes. However, no such population is detected. There-

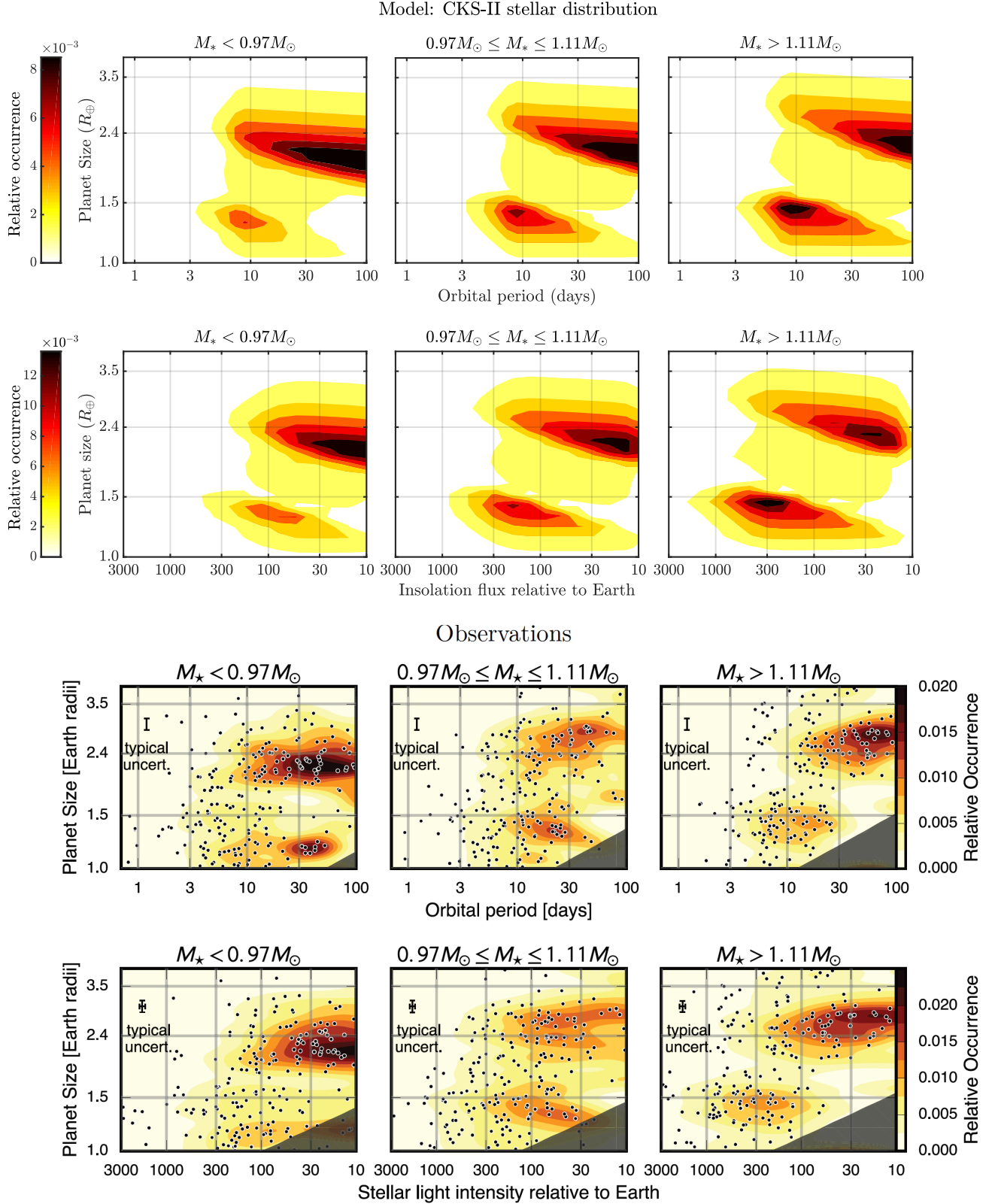


**Figure 4.** Comparison of core-powered mass-loss results (top two rows) with observations (bottom two rows) from [Fulton & Petigura \(2018\)](#) (reproduced with permission). The planet size distribution is shown for three stellar mass bins as a function of orbital period (first and third row) and stellar insolation flux (second and fourth row). Our core-powered mass-loss results clearly show that the radius valley moves to larger planet sizes for more massive stars (see also Figure 3). In addition, we find that the super-Earth and sub-Neptune populations move to higher stellar insolation for more massive stars, which is due to the fact that the exoplanet period distribution is approximately independent of stellar mass.

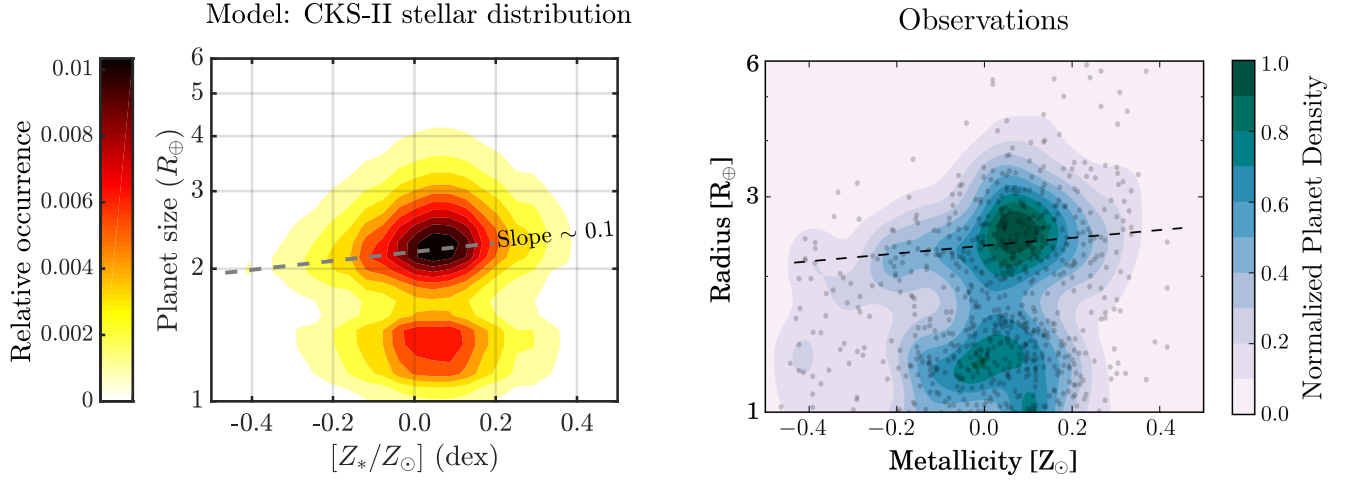


**Figure 5.** Comparison of core-powered mass-loss results as a function of metallicity,  $[Z_*/Z_\odot]$ , (left panel) with observations from [Owen & Murray-Clay \(2018\)](#) (right panel). The dashed lines in both panels indicate the increase in the size of sub-Neptunes with metallicity with a slope of  $d \log R_p / d \log Z_* \sim 0.1$ . Sub-Neptunes are on average larger around metal-rich stars, since higher atmospheric opacities result in longer thermal contraction and cooling timescales. In contrast, the location and slope of the radius valley, as well as the average sizes of super-Earths are, to first order, independent of metallicity; see Section 5.2 for details.

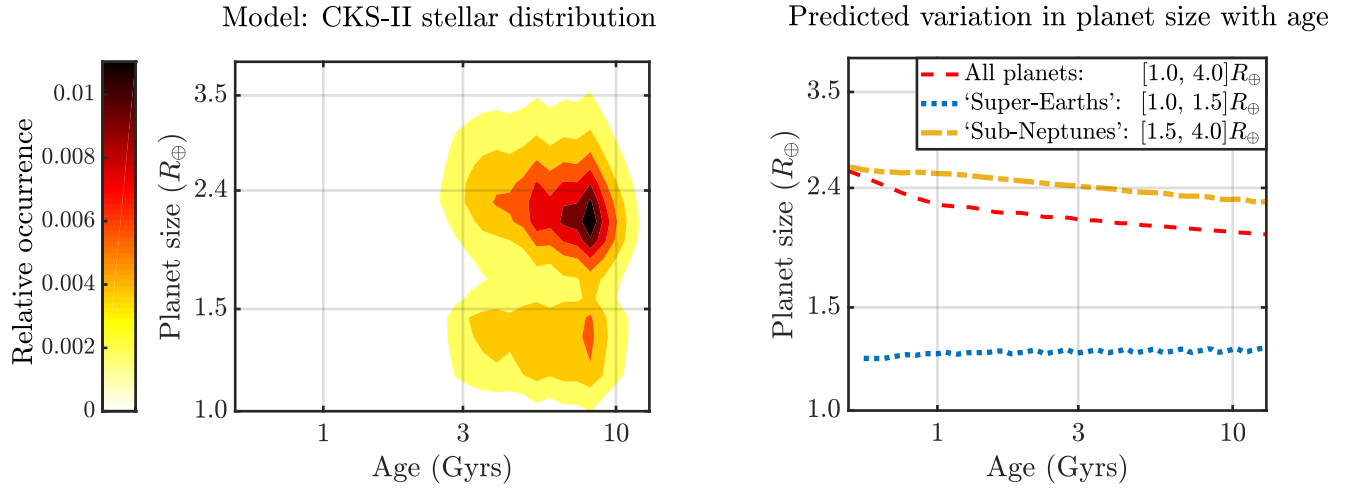


**Figure 6.** Core-powered mass-loss results as a function of age. The left panel shows results for a planet population around a distribution of host stars modeled after the CKS-II dataset ([Johnson et al. 2017](#)); the right panel shows our predicted average planet size with age. These results demonstrate that the average size of sub-Neptunes decreases significantly while the average size of super-Earths increases slightly with age. In addition, we predict that the relative occurrence of sub-Neptunes with respect to super-Earths decreases with age over Gyr timescales. These trends are due to the fact that typical mass-loss timescales are on the order of 0.5-1 Gyrs, which leads to an increase of super-Earths with respect to sub-Neptunes over these timescales. In addition the envelopes of sub-Neptunes will have had more time to cool and contract resulting in a decrease in the average sub-Neptune size with age; see Section 5.3 and Figure 9 for details.

fore, this observed shift in insolation is unlikely a signature of an atmospheric mass-loss mechanism. Instead, Figures 18 and 19 from [Hirano et al. \(2018\)](#) might be evidence of proto-planetary disk truncation around M-dwarfs which could be caused by photoevaporation, or some other process.

The left panel of Figure 5 shows core-powered mass-loss results as a function of stellar metallicity. We find that the size of sub-Neptunes increases with increasing stellar metallicity whereas neither the radius valley nor population of super-Earths show any visually discernible dependence on stellar metallicity. Specifically, we find that the average size of sub-Neptunes increases with stellar metallicity (represented by the inclination of the contours of the

sub-Neptune population) such that  $d \log R_p / d \log Z_* \sim 0.1$ . These findings are consistent with observations by [Petigura et al. \(2018\)](#), [Dong et al. \(2018\)](#) and [Owen & Murray-Clay \(2018\)](#). The right panel of Figure 5 shows observations from [Owen & Murray-Clay \(2018\)](#) based on the CKS-II dataset ([Johnson et al. 2017](#)). The dashed line, roughly drawn to indicate the observational trend of planet size with stellar metallicity for the sub-Neptune population, has a slope of  $d \log R_p / d \log Z_* \sim 0.1$ . We note here that there is hardly any change in the location of the valley as a function of stellar metallicity. This suggests that, to first order, changes in metallicity predominately impact the sizes of sub-Neptunes but not the super-Earth population. As we show in the next



section, this observation can be easily understood in the context of core-powered mass-loss mechanism, which predicts no metallicity dependence of the radius valley and the super-Earth population (Gupta & Schlichting 2019) but increasing planet sizes for the sub-Neptune population as their thermal contraction and cooling timescales are prolonged for higher metallicities as these correspond to larger envelope opacities.

Figure 6 shows core-powered mass-loss results as a function of age for a population of planets with host stars modeled after the CKS-II dataset (Johnson et al. 2017). We find that sub-Neptunes are visibly smaller around older stars since their envelopes had more time for thermal contraction in older systems, whereas super-Earths have similar but slightly larger sizes as a function of age. Given the small range in stellar ages and their relatively larger uncertainties, no direct statistical comparison between core-powered mass-loss results and observations is currently possible (but see discussion in section for 5.3 details).

In this section we have shown a comparison of our core-powered mass-loss results for a population of planets with host stars modeled after the CKS-II dataset and shown that the core-powered mass-loss mechanism can reproduce a multitude of the observational trends (e.g., Fulton & Petigura 2018; Owen & Murray-Clay 2018; Petigura et al. 2018; Dong et al. 2018; Wu 2019). In the next section, we explain the key physical properties of the core-powered mass-loss mechanism that lead to the results presented here and make observational predictions for the core-powered mass-loss mechanism as a function of stellar properties.

## 5 RESULTS: ANALYTICAL SCALINGS & DEPENDENCE ON STELLAR PROPERTIES

In this section, we explore and explain, analytically and numerically, the dependence of the core-powered mass-loss mechanism on stellar mass, metallicity and age by only varying one of these stellar parameters at a time.

We assume, with the exception of Section 5.4, the same planet mass and orbital period distribution for all host stars such that any changes in the resulting planet size distribution can be unambiguously attributed to changes in the host star properties. Unlike in Section 4, where we modeled the host stars after the CKS-II dataset, we assume a uniform distribution for the single stellar parameter that we are varying. For the parameters that are held constant, we assume solar values for metallicity and mass, and an age of 3 Gyrs.

### 5.1 Dependence on stellar mass

Stellar mass plays a role when modelling atmospheric loss driven by the core-powered mass-loss mechanism in two ways: (i) it relates the orbital period distribution of the planet population to the semi-major axis and (ii) it dictates the equilibrium temperature  $T_{eq}$  for each planet given its distance from the host star. The equilibrium temperature depends on the bolometric luminosity  $L_*$  and the semi-major axis  $a$  such that  $T_{eq} \propto L_*^{1/4} a^{-1/2}$ . The bolometric luminosity, in turn, can be expressed as  $L_* \propto T_{eff}^4 R_*^2$ , where  $T_{eff}$  is the effective temperature of the star and  $R_*$  the stellar

radius. The CKS-II dataset provides both, stellar radii and effective temperatures. However, the bolometric luminosity is also strongly correlated with the stellar mass  $M_*$  such that

$$L_*/L_\odot = (M_*/M_\odot)^\alpha, \quad (16)$$

where  $\alpha \sim 4 - 6$  for  $0.5 < M_* < 2.0$  (e.g., Eker et al. 2018). This relation also holds for the CKS-II dataset for which we find that it is best described by  $\alpha \approx 5$ . The dependence of the core-powered mass-loss mechanism on stellar mass is therefore, to first order, driven by the stellar mass-luminosity relation, since more massive stars have higher luminosity which leads to higher  $T_{eq}$  and hence more mass loss from the planet.

While we directly use stellar radius and effective temperature to derive a star's luminosity for the numerical simulation results discussed in Section 4, in this section we use the stellar mass-luminosity relation with  $\alpha = 5$  to isolate the effect of stellar mass on the resulting radius valley and planet size distribution. Given the stellar mass-luminosity relation, for a fixed period distribution we get  $T_{eq} \propto M_*^{(\alpha/4)-(1/6)}$ , which sets the temperature at the planet's Bondi radius. Gupta & Schlichting (2019) showed that the slope and location of the valley in the planet distribution is set by the condition  $t_{loss}^B = t_{cool}$ . Furthermore, they showed that this condition is very well approximated by  $GM_p/c_s^2 R_{rcb} = \text{constant}$ , due to the exponential dependence of  $t_{loss}^B$  (see Section 2). Substituting for the speed of sound, the mass-radius relation of the core, and using the fact that  $R_{rcb} = R_p \approx 2R_c$  yields

$$R_p^3 T_{eq}^{-1} \approx \text{constant}. \quad (17)$$

Substituting for  $T_{eq}$  using the stellar mass-luminosity relation we find

$$\frac{d \log R_p}{d \log M_*} = \frac{3\alpha - 2}{36} = 0.36 \text{ for } \alpha = 5. \quad (18)$$

This analytical estimate of the slope is in good agreement with the observations which find  $d \log R_p / d \log M_* \sim 0.35$  (e.g., Fulton & Petigura 2018; Wu 2019) and with the results of our numerical simulations discussed in Section 4 and shown in Figure 7. In addition, we predict that, if planetary evolution is dominated by core-powered mass-loss, the radius valley will have a slope  $d \log R_p / d \log M_* = (3\alpha - 2)/36$  and hence will be steeper for planets around host stars with larger  $\alpha$  and vice-versa (e.g., Eker et al. 2018). This trend would be weakened if photoevaporation or other mass-loss processes also play a significant role in shaping the exoplanet radius distribution.

Figure 7 displays the planet size distribution as a function of stellar mass (luminosity) assuming that all host stars are 3 Gyrs old and have solar metallicity. The left panel of Figure 7 shows the location of the valley and the size of super-Earths and sub-Neptunes increases with increasing stellar mass (or luminosity) as derived analytically in Equation (18) and as shown by the black-dashed line in the figure. In other words, planets around more massive stars are, on average, bigger in size. In addition, the relative abundance of sub-Neptunes decreases and that of super-Earths increases with increasing stellar mass. This is because planets around more massive or luminous stars are more susceptible to losing their atmospheres as they have higher equilibrium tem-

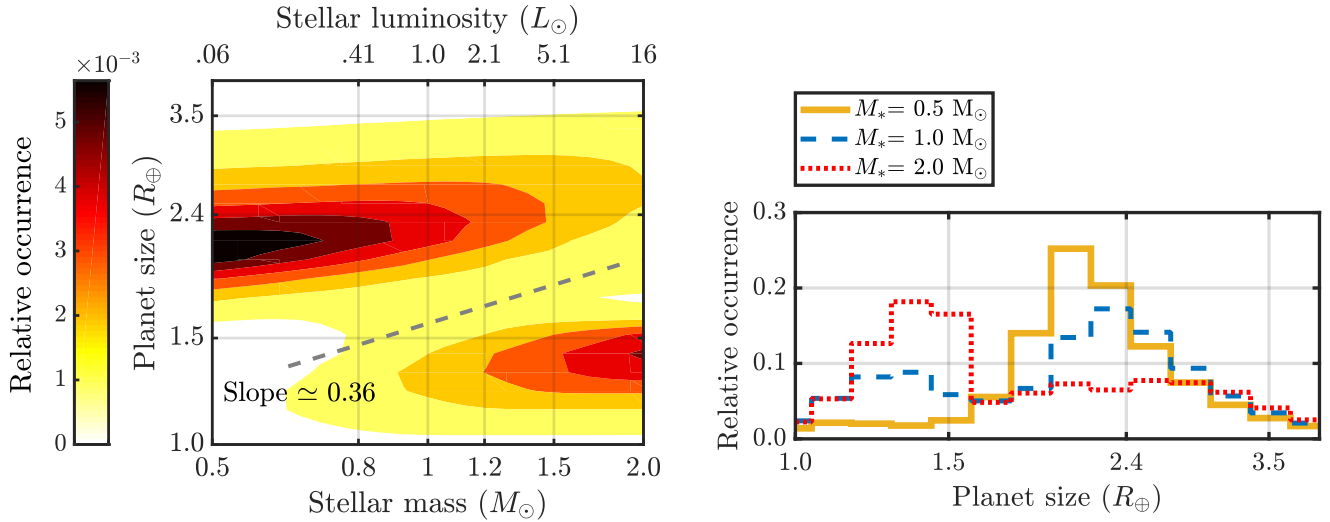


**Figure 7.** Core-powered mass-loss results as a function of stellar mass (luminosity) for planets around solar metallicity stars after 3 Gyrs of thermal evolution and mass-loss. Here, only the stellar mass is varied while keeping all other parameters the same. The left panel shows the two-dimensional distribution of planet size as a function of stellar mass (luminosity); the right panel displays the corresponding histograms of planet sizes for stellar masses of  $0.5M_{\odot}$  (yellow-solid line),  $1M_{\odot}$  (blue-dashed line), and  $2M_{\odot}$  (red-dotted line), respectively. The dashed line in the left panel corresponds to the slope of the radius valley,  $d \log R_p / d \log M_* \approx 0.36$ , derived analytically in Equation (18)

peratures which result in shorter mass-loss timescales and thus a higher fraction of sub-Neptunes become super-Earths around more massive stars. These two results are also evident from the right panel of Figure 7 which shows the radius distribution for host star masses corresponding to  $0.5M_{\odot}$ ,  $1.0M_{\odot}$  and  $2.0M_{\odot}$ , respectively.

These results explain observations reported by [Fulton & Petigura \(2018\)](#) and [Wu \(2019\)](#) who find that the radius valley increases in planet size with increasing stellar mass. Assuming that the orbital period distribution is independent of stellar mass, this observation seems surprising under a basic framework of photoevaporation since the XUV flux roughly remains constant as a function of stellar mass and hence should yield an approximately flat radius valley as a function of host star mass (see also [Wu 2019](#)). This is because the ratio of XUV to bolometric flux decreases with stellar mass (e.g., [Jackson et al. 2012](#); [Tu et al. 2015](#)) while the bolometric flux increases. These two trends roughly cancel each other ([Owen & Murray-Clay 2018](#)). Therefore, in order to explain radius valley’s dependence on stellar mass with photoevaporation models, [Wu \(2019\)](#) invoked a linear correlation between the planet mass distribution and host star mass.

As shown above and in Section 4, the core-powered mass-loss mechanism yields a shift in the radius valley to larger planet sizes around more massive stars with a slope given by  $d \log R_p / d \log M_* \approx 0.35$ , in agreement with observations. We therefore find, contrary to photoevaporation models, no evidence for a correlation between planet and stellar mass. We nonetheless investigate the imprint that a linear correlation between planet and stellar mass would have on the observed planet size distribution in the context of the core-powered mass-loss mechanism in Section 5.4.

## 5.2 Dependence on stellar metallicity

The rate at which planets cool and contract depends on the opacity of the envelope,  $\kappa$ , as this sets the rate of radiative diffusion through the radiative-convective boundary (see Equations (6) and (8)). If the opacity at the radiative-convective boundary is proportional to the stellar metallicity,  $Z_*$ , as we assume in Section 2, then the planetary cooling timescale is directly proportional to the stellar metallicity such that  $t_{cool} \propto Z_*$ . In other words, a planet around a metal-poor star, i.e., a planet with lower atmospheric opacity, loses its energy on a shorter timescale than around a higher metallicity star. As a result, sub-Neptunes will be larger around higher metallicity stars than metal poor stars when comparing systems of the same age. We can derive an analytical estimate for the size of sub-Neptunes as a function of metallicity by assuming that atmospheric mass-loss can be neglected such that  $M_{atm} = \text{constant}$  and thus cooling and contraction due to mass-loss can be ignored. In this case, Equations (1), (2) and (5) to (7) can be combined to yield

$$t \propto Z_* \Delta R^{-\frac{\beta\gamma+1}{\gamma-1}}, \quad (19)$$

where  $t$  is the age of the system and where we used Equation (1) and the assumption that  $M_{atm} = \text{constant}$  to eliminate the dependence on the density at the  $R_{rcb}$ . Hence, from Equation (19) we have that at a given time  $\Delta R \propto Z_*^{(\gamma-1)/(\beta\gamma+1)}$  such that

$$\frac{d \log R_p}{d \log Z_*} = \frac{\Delta R}{R_p} \left( \frac{\gamma-1}{\beta\gamma+1} \right) \approx \frac{5}{46}, \quad (20)$$

where we substitute  $\gamma = 7/5$ ,  $\beta = 0.6$  (see Equation (7)) and  $\Delta R/R_p \approx 1/2$  in the last step. We note here that approximating  $\Delta R/R_p$  as  $\approx 1/2$ , which is essentially our initial condition, results in the maximum slope possible and since

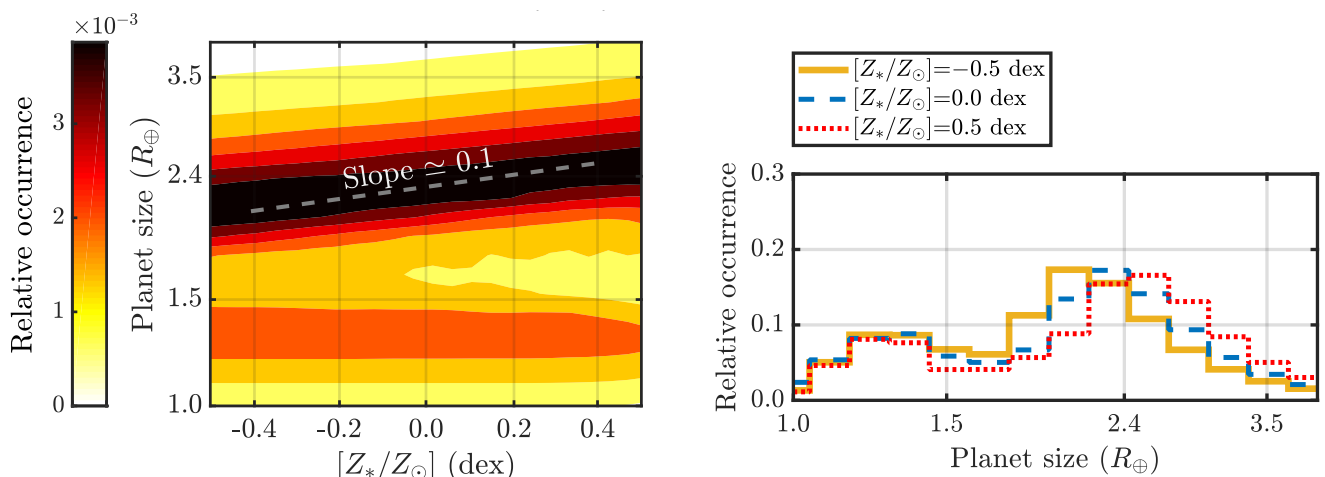


**Figure 8.** Core-powered mass-loss results as a function of stellar metallicity for planets around solar mass stars after 3 Gyrs of thermal evolution and mass-loss. The left panel shows the distribution of planet size as a function of metallicity  $\equiv [Z_*/Z_\odot]$ ; the right panel displays the corresponding histograms of planet size for metallicities of  $-0.5$  dex (yellow-solid line),  $0.0$  dex (blue-dashed line), and  $0.5$  dex (red-dotted line), respectively. The gray-dashed line in the left-panel shows the increase in the size of sub-Neptunes with metallicity, i.e.,  $d \log R_p / d \log Z_* \approx 0.1$ , derived analytically in Equation (20). In contrast to the sub-Neptune population, the location of the valley, specifically the lower edge of the valley defining the upper envelope of the super-Earth population, shows no significant dependence on metallicity. Furthermore, this figure also shows that the relative occurrence of sub-Neptunes with respect to super-Earths increases with increasing metallicity.

$\Delta R/R_p$  decreases over time as the envelope cools and contracts. The value calculated in Equation (20) is therefore an overestimate of the slope for a planet population with an age of 3 Gyrs.

The left panel of Figure 8 shows the planet size distribution as a function of metallicity, where we assume that the planet’s opacity scales linearly with stellar metallicity (see Equation (7)). The size trend with metallicity and slope of the sub-Neptune population from our numerically evolved planet population agrees well with the simple analytical estimate derived in Equation (20) above. In addition, this analytical scaling matches the observations and our numerical results discussed in Section 4 where  $d \log R_p / d \log Z_* \sim 0.1$  (Owen & Murray-Clay 2018, see also Figure 5). Our results are also consistent with observations reported by Dong et al. (2018), Owen & Murray-Clay (2018) and Petigura et al. (2018) who all find that sub-Neptunes are larger around more metal-rich stars. Our results similarly apply to M-dwarfs and can explain observations that find that planets, on average, are larger around higher metallicity M-dwarfs (Hirano et al. 2018). These results are also evident from the right panel of Figure 8 which shows the planet size distribution for host star metallicities of  $-0.5$ ,  $0.0$  and  $0.5$  dex, respectively.

In contrast to the sub-Neptune population, core-powered mass-loss predicts a negligible dependence of the location of the radius valley and sizes of super-Earths as a function of metallicity. This is because, as shown in Gupta & Schlichting (2019) and summarized in Section 5.1, the slope of the radius valley is, to first order, given by  $GM_p / c_s^2 R_{rcb} = \text{constant}$ . Therefore, as long as the spontaneous mass-loss phase (boil-off phase) results in initial planet sizes  $R_{rcb} = R_p \approx 2R_c$  independent of envelope metallicity, we find that the slope of the valley, especially the lower edge that marks the upper envelope of the super-Earth population, does not depend on metallicity. This explains the almost flat contours

of the super-Earth population shown in Figure 8 and the flat valley shown in Figure 5 and is the reason why, to first order, only the sizes of sub-Neptunes depend on stellar metallicity but not the location of the valley or the sizes of super-Earths (see Figures 5 and 8).

In reality, there is a weak dependence of the radius valley and super-Earth sizes on metallicity because the atmospheric mass-loss timescales increase with stellar metallicity such that at a given time, planets with higher atmospheric opacities will have lost less of their envelopes than those with lower envelope opacities. This leads, for a given age, to smaller cores (super-Earths) around metal-rich stars compared to metal poor ones. This in addition implies that, at a given time, the relative abundance of super-Earths to sub-Neptunes should be higher around lower metallicity stars, as can be seen in Figure 8. These results offer an explanation as to why the relative occurrence of sub-Neptunes increases with increasing metallicity as found observationally by Petigura et al. (2018) and Dong et al. (2018).

### 5.3 Dependence on stellar age

Atmospheric mass-loss driven by the cooling of the underlying core depends on the age of the system as mass-loss and thermal evolution extend, in contrast to photoevaporation, over Gyr timescales (see Section 2 for details). This implies that sub-Neptunes around older stars will be smaller than those around younger stars since the former will have had more time to cool and contract. Moreover, planets that eventually become super-Earths have had more time to complete their mass loss in older systems. Thus, older stars will have a higher abundance of super-Earths relative to sub-Neptunes compared to younger stars. Specifically, we expect a drastic change in the planet size distribution between stars that are younger and older than the typical core-powered mass-loss timescale, which is of the order of a Gyr. Due to these long

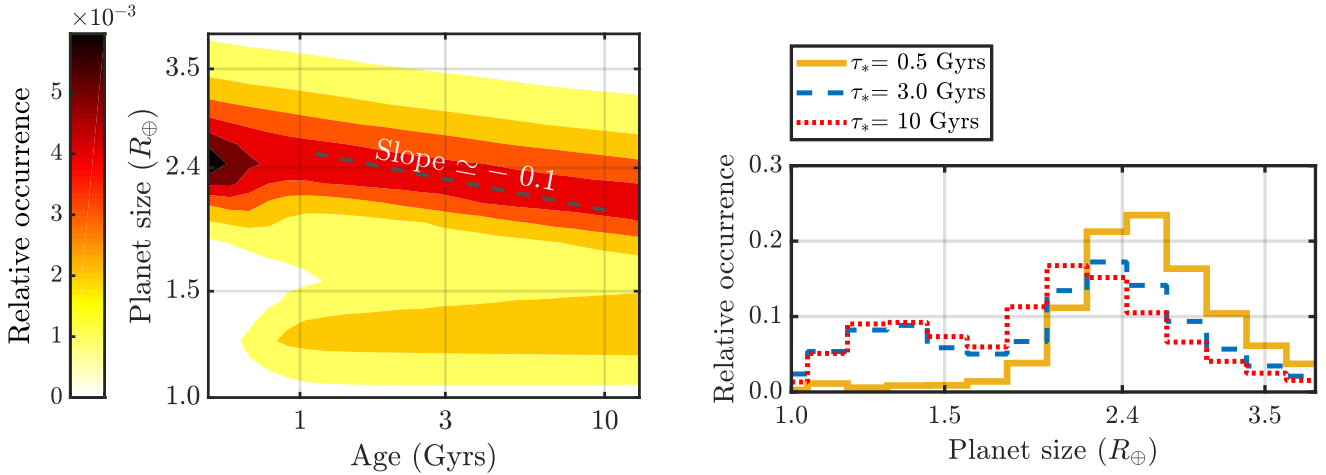


**Figure 9.** Core-powered mass-loss results as a function of stellar age for planets with solar mass and solar metallicity host stars. The left panel shows the distribution of planet sizes as a function of age; the right panel displays the corresponding histograms of planet size for ages of 0.5 Gyrs (yellow-solid line), 3.0 Gyrs (blue-dashed line), and 10 Gyrs (red-dotted line), respectively. The dashed line in the left panel shows the decrease in the size of sub-Neptunes with age, i.e.,  $d \log R_p / d \log \tau_* \approx -0.1$ , derived analytically in Equation (21). In contrast to the sub-Neptunes, the average size of super-Earths increases with age. In addition, this figure shows that the relative abundance of super-Earths to sub-Neptunes increases over time, as expected.

mass-loss timescales, we predict the transformation of sub-Neptunes into super-Earths to continue over Gyr timescales.

Assuming a constant metallicity, we have from Equation (19) that the radii of the sub-Neptune population vary with age as

$$\frac{d \log R_p}{d \log \tau_*} = -\frac{\Delta R}{R_p} \left( \frac{\gamma - 1}{\beta \gamma + 1} \right) \approx -\frac{5}{46}, \quad (21)$$

where we again substitute  $\gamma = 7/5$ ,  $\beta = 0.6$  and  $\Delta R / R_p \approx 1/2$  in the last step. Just like for the metallicity dependence, the value calculated in Equation (21) is an overestimate of the slope for a planet population with an age of 3 Gyrs (see discussion following Equation (20) for details). Nonetheless, this analytical estimate agrees with our numerical results shown in Figure 9.

The left panel of Figure 9 shows the changes in planet size as a function of age for solar mass and solar metallicity host stars. As expected, sub-Neptunes decrease in size with increasing stellar age as their envelopes cool and contract. In addition, we find an increase in the average size of super-Earths with age as larger (more massive) cores are being stripped of their envelopes over time. This, in addition, leads to an increase in the number of super-Earths relative to sub-Neptunes with time. These results are displayed in the right panel of Figure 9 which shows the planet size distribution for host stars with ages of 0.5, 3.0 and 10.0 Gyrs. The core-powered mass-loss mechanism therefore predicts that sub-Neptunes decrease in size, while the average size of super-Earths increases with stellar age and that the relative abundance of super-Earths with respect to sub-Neptunes increases with time, especially over periods from 500 Myrs to 3 Gyrs.

The relatively large uncertainties in most stellar ages currently do not allow for a detailed comparison between predictions from the core-powered mass-loss mechanism and observations. However, according to Mann et al. (2016) and other ZEIT studies, younger planets (in stellar clusters  $\sim 10$ -650 Myrs old) are on average bigger than the older *Ke*-

pler planets ( $\gtrsim 1$  Gyr old); see Figure 12 in Rizzuto et al. (2018). According to these studies, close-in planets likely lose significant portions of their atmospheres even after the first few hundred million years. If correct, these observations directly confirm predictions from core-powered mass-loss with its Gyr-long mass-loss timescales (Ginzburg et al. 2016) and would be challenging to explain with photoevaporation which mostly occurs over the first 100 Myrs.

#### 5.4 Investigating proposed correlations between the planet- and stellar-mass distributions

As discussed above, to reconcile the observed correlation between the location of the radius valley with stellar mass considering only atmospheric-loss due to photoevaporation, Wu (2019) had to invoke a linear correlation between the planet- and stellar-mass distributions. Specifically, she inferred that the peak of the planet mass distribution, i.e.,  $\sigma_M$  (see Equation (15)), scales linearly with the mass of the host star.

In Sections 4 and 5.1, we demonstrate that no such correlation is required when accounting for planetary evolution and atmospheric loss driven by the core-powered mass-loss mechanism. In other words, we find that in order to explain the observations we don't need to impose a positive correlation between the planet- and stellar-mass distribution as inferred by Wu (2019). Nevertheless, in this section we investigate how our core-powered mass-loss results would change if we impose a linear relation between the planet- and stellar-mass distribution. Specifically, we assume that  $\sigma_M / 3M_{\oplus} = M_* / M_{\odot}$  (see Equation (15) for details).

Figure 10 demonstrates that the slope of the valley increases when we assume a linear relation between the planet- and stellar-mass distributions (middle panel in Figure 10) compared to a planet-mass distribution that is independent of stellar mass (left panel in Figure 10). In fact, the increase is so significant that it becomes inconsistent with the observations (right panel in Figure 10). This result implies



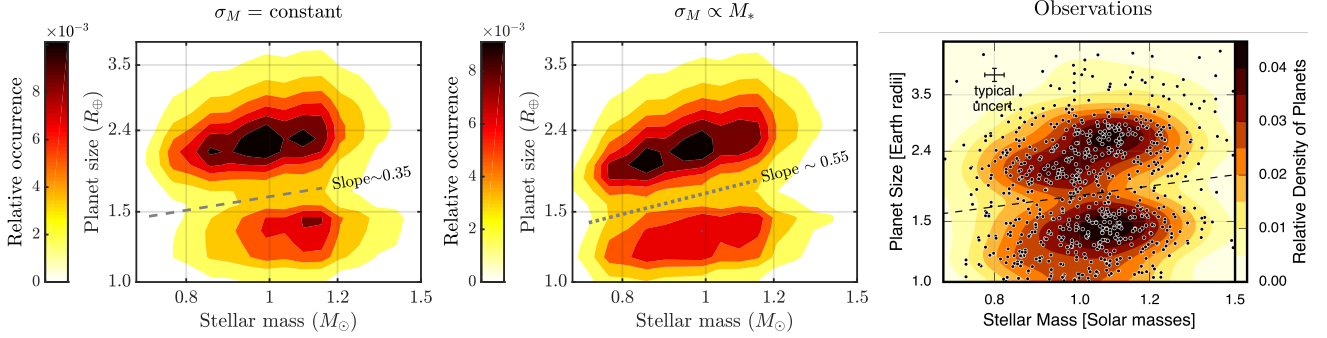


**Figure 10.** Comparison of core-powered mass-loss results (left and middle panel) with observations from [Fulton & Petigura \(2018\)](#) (right panel). The left and middle panel show the resulting planet size distribution assuming no correlation between planet- and stellar-mass (left) and for a linear correlation between the planet- and stellar-mass distributions (middle), respectively.  $\sigma_M$  corresponds to the peak in the planet mass distribution (see Equation (15) for details). The lines indicate the slopes of the radius valley which are given by  $d \log R_p / d \log M_* \approx 0.35$  (dashed-line, left panel) and  $d \log R_p / d \log M_* \approx 0.55$  (dotted-line, middle panel) for the cases without and with a linear correlation between the planet- and stellar-mass distributions, respectively. Comparing the right with the left panel shows that assuming a linear scaling between the planet- and stellar-mass distributions results in a slope of the radius valley that is significantly steeper ( $d \log R_p / d \log M_* \approx 0.55$ ) than the observations ( $d \log R_p / d \log M_* \approx 0.35$ ). Core-powered mass-loss suggests that there is no significant correlation between the planet- and stellar-mass distributions. The age, metallicities and masses of the host stars are modeled after the stellar distributions from the CKS-II dataset ([Johnson et al. 2017](#)).

that, if the core-powered mass-loss mechanism is primarily responsible for sculpting the radius valley and its observed dependence on stellar mass, then the underlying planet-mass distribution should, to first order, have no dependence on the mass of the host star. Determining the true underlying exoplanet mass distribution and comparing it for different stellar masses therefore provides a unique opportunity to observationally determine whether photoevaporation or core-powered mass-loss is predominantly responsible for sculpting the radius valley.

## 6 DISCUSSION AND CONCLUSIONS

In this paper we extended previous work on the core-powered mass-loss mechanism ([Ginzburg et al. 2018](#); [Gupta & Schlichting 2019](#)), and investigated how stellar mass, metallicity and age impact the resulting planet size distribution.

We first investigated the evolution of planets around a population of host stars modeled after the CKS-II dataset ([Johnson et al. 2017](#)). This allows for a direct comparison between our core-powered mass-loss results and observations based on the CKS-II data set. We find that, to first order, the resulting planet size distribution as a function of period and/or stellar insolation is very similar to that obtained by [Gupta & Schlichting \(2019\)](#), who only modeled ‘Sun-like’ host stars. However, modeling the actual host star properties yields, as expected, an even higher degree of agreement between core-powered mass-loss results and the observations ([Fulton & Petigura 2018](#)). In addition, we find that our core-powered mass-loss results are in excellent agreement with the observed planet size distribution as a function of both stellar mass (e.g., [Fulton & Petigura 2018](#); [Wu 2019](#)) and metallicity (e.g., [Owen & Murray-Clay 2018](#); [Petigura et al. 2018](#); [Dong et al. 2018](#); [Hirano et al. 2018](#)). Furthermore, our results also explain the shift in the planet size distribution to higher insolation flux as a function of stellar mass, as observed by [Fulton & Petigura \(2018\)](#).

In addition, we investigated how our core-powered mass-loss results depend on stellar mass, metallicity and age separately. This enabled us not only to understand the key physical processes responsible for the agreement of our results with observations, but also enables us to make predictions for the planet size distribution and its dependence on a wide range of stellar parameters.

We find that the planet size distribution varies with stellar mass because core-powered mass-loss depends on the bolometric luminosity which, in turn, is strongly correlated with stellar mass. Thus, more massive stars host planets with higher equilibrium temperature, making even more massive planets susceptible to complete atmospheric loss. We derived an analytical estimate for the slope of the valley in planet size and stellar mass parameter space and show that  $d \log R_p / d \log M_* \approx (3\alpha - 2)/36$ , where  $\alpha$  is the power-law index relating stellar mass and luminosity, such that  $L_*/L_\odot = (M_*/M_\odot)^\alpha$ . We find that  $\alpha \approx 5$  for the host stars in the CKS-II dataset and use this to calculate that  $d \log R_p / d \log M_* \approx 0.36$ . This analytical estimate is in good agreement with our numerical results and the observations ([Fulton & Petigura 2018](#); [Wu 2019](#)).

In contrast to stellar mass, we find that, to first order, that the core-powered mass-loss mechanism predicts a negligible dependence of the location of the radius valley as a function of metallicity and age. This is because, as shown in [Gupta & Schlichting \(2019\)](#) and summarized in Section 5.1, the slope of the radius valley is, to first order, given by  $GM_p/c_s^2 R_{rcb} = \text{constant}$ , which has no explicit dependence on metallicity or age. Therefore, as long as the spontaneous mass-loss phase (boil-off phase) results in initial planet sizes  $R_{rcb} = R_p \approx 2R_c$  independent of envelope metallicity or age, we have that the slope of the valley, especially the lower edge that marks the upper contour of the super-Earth population, does not depend on metallicity or age. In reality, there is a weak dependence on age and metallicity resulting in slightly larger cores that are stripped as a function of time (see Figure 9) and slightly smaller cores that are stripped of their atmospheres as a function of metallicity (see Figure 8). This

dependence is due to the metallicity's effect on the mass-loss timescale. However, since this metallicity dependence does not appear in the exponent of the mass-loss timescales, the metallicity and hence age dependence is only a second-order effect and hence weak.

Unlike the location and slope of the radius valley, the size distribution of the sub-Neptune population does display a visible dependence on both metallicity and age. This is because the rate at which the envelope cools and contracts is related to its opacity. The size of sub-Neptunes therefore depends on both the opacity of the envelope and the age of the system. Assuming that the envelope opacity is proportional to the stellar metallicity, the cooling timescale is directly proportional to the stellar metallicity. As a result, sub-Neptunes will be larger around higher metallicity and/or younger stars than metal poor and/or older stars. We derived an analytical estimate for the size of sub-Neptunes as a function of metallicity and age and showed that  $d \log R_p / d \log Z_* \simeq 0.1$  and  $d \log R_p / d \log \tau_* \simeq -0.1$ , respectively. Both of these analytical estimates are in agreement with our numerical results. In addition, the former is in good agreement with the observations of sub-Neptunes around metal-rich FGK stars (Owen & Murray-Clay 2018; Dong et al. 2018; Petigura et al. 2018) and M-dwarfs (Hirano et al. 2018); no direct comparison with observations can yet be made for the latter.

Although we just discussed here the dependence of the core-powered mass-loss mechanism on stellar mass, metallicity and age in isolation, some of these trends can be more pronounced in the observations because, for example, in the CKS-II dataset more massive stars are on average younger and more metal-rich.

## 6.1 Observational test: Distinguishing between core-powered mass-loss and photoevaporation signatures

Although both photoevaporation and core-powered mass-loss can explain the observed radius valley in the exoplanet size distribution and both mechanisms are likely to operate in conjunction in many systems, their different timescales and difference dependencies on stellar properties provide a set of observational predictions that allow for the determination of their relative importance. Specifically, we make the following observational predictions:

### 6.1.1 Correlations between planet- and stellar-mass

Our core-powered mass-loss results predict no significant, i.e., weaker than linear, correlation between the mass of the host star and the planet mass distribution. We therefore expect that observationally measured planet mass distributions will be, to first order, independent of stellar mass. In contrast, photoevaporation models, based on work by Wu (2019), predict a linear scaling between the planet mass distribution and the mass of the host star.

### 6.1.2 Slope of the radius valley as a function of stellar mass (or luminosity)

Since the positive correlation between the location of the radius valley with stellar mass is mainly due to the stellar mass-luminosity relation, the core-powered mass-loss model can be tested by examining the slope of the radius valley for different stellar masses. For example, as shown above, the slope of the radius valley as a function of stellar mass is given by  $d \log R_p / d \log M_* = (3\alpha - 2)/36$ , where  $L_*/L_\odot = (M_*/M_\odot)^\alpha$ . The slope will therefore be steeper for planets around host stars with larger  $\alpha$  and vice-versa. Best of all, one can examine planets around two host star populations with different  $\alpha$  ( $\alpha$  can be directly determined from the host stars in the sample) and check for the predicted change in slope of the radius valley as a function of stellar mass (or luminosity).

### 6.1.3 Relative abundance of super-Earths and sub-Neptunes as a function of age

Since atmospheric mass-loss driven by the core-powered mass-loss mechanism proceeds over Gyr timescales, we predict that the relative abundance of super-Earths with respect to sub-Neptunes increases with age. Specifically, we expect the abundance of super-Earths to continue to increase significantly after 500 Myrs, since typical atmospheric mass-loss timescales are of the order of a Gyr. In contrast, since photoevaporation is driven by the X-ray and EUV radiation from the host star, which declines drastically after the first 100 Myrs, the relative abundance of super-Earths should remain constant after the first 100 Myrs. Photoevaporation models therefore predict no significant increase in the super-Earth population after the first 100-200 Myrs.

### 6.1.4 Planets in the gap

Since planets continue to lose mass over Gyr timescales, the core-powered mass-loss mechanism predicts that some planets will be still be losing mass today. Observationally these planets can be caught as they cross the radius valley, i.e. they maybe found inside the gap. In addition, atmospheric mass-loss may be directly detectable observationally.

## 6.2 Outlook

In this work we have shown how planetary evolution under the core-powered mass-loss mechanism can explain many of the observed features of the distribution of small, short-period exoplanets and their dependence on stellar properties. Although we have just summarized a list of observational test that should be able to distinguish between signatures imprinted on the exoplanet population by photoevaporation and core-powered mass-loss, we would like to emphasize that it appears almost inevitable that both processes take place to some extent. We therefore suspect that they both play a role in shaping the observed super-Earth and sub-Neptune populations. To that end, we plan to combine photoevaporation and core-powered mass-loss models in future work. Combining both of these mass-loss mechanisms may turn out to be crucial for correctly inferring physical

properties (e.g., core densities) of the exoplanet population from the observations.

## ACKNOWLEDGEMENTS

We thank the California-*Kepler* Survey team for making their data publicly available. H.E.S. gratefully acknowledges support from the National Aeronautics and Space Administration under grant No. 17 XRP17\_2 – 0055 issued through the Exoplanet Research Program.

## REFERENCES

- Berger T. A., Huber D., Gaidos E., van Saders J. L., 2018, *ApJ*, **866**, 99
- Borucki W. J., et al., 2010, *Science*, **327**, 977
- Bower D. J., Kitzmann D., Wolf A. S., Sanan P., Dorn C., Oza A. V., 2019, arXiv e-prints, p. [arXiv:1904.08300](https://arxiv.org/abs/1904.08300)
- Brown T. M., Latham D. W., Everett M. E., Esquerdo G. A., 2011, *AJ*, **142**, 112
- Carter J. A., et al., 2012, *Science*, **337**, 556
- Chen H., Rogers L. A., 2016, *ApJ*, **831**, 180
- Dong S., Xie J.-W., Zhou J.-L., Zheng Z., Luo A., 2018, *Proceedings of the National Academy of Science*, **115**, 266
- Eker Z., et al., 2018, *MNRAS*, **479**, 5491
- Fortney J. J., Marley M. S., Barnes J. W., 2007, *ApJ*, **659**, 1661
- Freedman R. S., Marley M. S., Lodders K., 2008, *ApJS*, **174**, 504
- Fressin F., et al., 2013, *ApJ*, **766**, 81
- Fulton B. J., Petigura E. A., 2018, *AJ*, **156**, 264
- Fulton B. J., et al., 2017, *AJ*, **154**, 109
- Ginzburg S., Schlichting H. E., Sari R., 2016, *ApJ*, **825**, 29
- Ginzburg S., Schlichting H. E., Sari R., 2018, *MNRAS*, **476**, 759
- Gupta A., Schlichting H. E., 2019, *MNRAS*, **487**, 24
- Hadden S., Lithwick Y., 2017, *AJ*, **154**, 5
- Hirano T., et al., 2018, *AJ*, **155**, 127
- Inamdar N. K., Schlichting H. E., 2015, *MNRAS*, **448**, 1751
- Jackson A. P., Davis T. A., Wheatley P. J., 2012, *MNRAS*, **422**, 2024
- Jin S., Mordasini C., 2018, *ApJ*, **853**, 163
- Jin S., Mordasini C., Parmentier V., van Boekel R., Henning T., Ji J., 2014, *ApJ*, **795**, 65
- Johnson J. A., et al., 2017, *AJ*, **154**, 108
- Lee E. J., Chiang E., 2015, *ApJ*, **811**, 41
- Lopez E. D., Fortney J. J., 2013, *ApJ*, **776**, 2
- Lopez E. D., Fortney J. J., 2014, *ApJ*, **792**, 1
- Mann A. W., et al., 2016, *ApJ*, **818**, 46
- Marcy G. W., Weiss L. M., Petigura E. A., Isaacson H., Howard A. W., Buchhave L. A., 2014a, *Proceedings of the National Academy of Science*, **111**, 12655
- Marcy G. W., et al., 2014b, *ApJS*, **210**, 20
- Martinez C. F., Cunha K., Ghezzi L., Smith V. V., 2019, *ApJ*, **875**, 29
- Owen J. E., Murray-Clay R., 2018, *MNRAS*, **480**, 2206
- Owen J. E., Wu Y., 2013, *ApJ*, **775**, 105
- Owen J. E., Wu Y., 2016, *ApJ*, **817**, 107
- Owen J. E., Wu Y., 2017, *ApJ*, **847**, 29
- Petigura E. A., Marcy G. W., Howard A. W., 2013, *ApJ*, **770**, 69
- Petigura E. A., et al., 2017, *AJ*, **154**, 107
- Petigura E. A., et al., 2018, *AJ*, **155**, 89
- Piso A.-M. A., Youdin A. N., 2014, *ApJ*, **786**, 21
- Rizzuto A. C., Vanderburg A., Mann A. W., Kraus A. L., Dressing C. D., Agüeros M. A., Douglas S. T., Krolkowski D. M., 2018, *AJ*, **156**, 195
- Rogers L. A., 2015, *ApJ*, **801**, 41

- Tu L., Johnstone C. P., Güdel M., Lammer H., 2015, *A&A*, **577**, L3
- Valencia D., O’Connell R. J., Sasselov D., 2006, *Icarus*, **181**, 545
- Van Eylen V., Agentoft C., Lundkvist M. S., Kjeldsen H., Owen J. E., Fulton B. J., Petigura E., Snellen I., 2018, *MNRAS*, **479**, 4786
- Weiss L. M., Marcy G. W., 2014, *ApJ*, **783**, L6
- Wu Y., 2019, *ApJ*, **874**, 91

This paper has been typeset from a  $\text{\TeX}$ / $\text{\LaTeX}$  file prepared by the author.